



# Mars' emitted energy and seasonal energy imbalance

Ellen Creecy<sup>a,1</sup> , Liming Li<sup>b,1</sup>, Xun Jiang<sup>a</sup>, Michael Smith<sup>c</sup>, David Kass<sup>d</sup>, Armin Kleinböhl<sup>d</sup>, and Germán Martínez<sup>e</sup>

Edited by Gerald Schubert, University of California, Los Angeles, CA; received November 19, 2021; accepted February 23, 2022

The radiant energy budget of a planet is essential to understanding its surface and atmospheric processes. Here, we report systematic measurements of Mars' emitted power, which are used to estimate the radiant energy budget of the red planet. Based on the observations from Mars Global Surveyor, Curiosity, and InSight, our measurements suggest that Mars' global-average emitted power is  $111.7 \pm 2.4 \text{ Wm}^{-2}$ . More importantly, our measurements reveal strong seasonal and diurnal variations of Mars' emitted power. The strong seasonal variations further suggest an energy imbalance at the time scale of Mars' seasons (e.g.,  $\sim 15.3\%$  of the emitted power in the Northern autumn for the Southern Hemisphere), which could play an important role in generating dust storms on Mars. We also find the 2001 global dust storm decreased the global-average emitted power by  $\sim 22\%$  during daytime but increased the global-average emitted power by  $\sim 29\%$  at nighttime. This suggests that global dust storms play a significant role in Mars' radiant energy budget.

Mars | energy budget | dust storms

The radiant energy budget, which is determined by the emitted thermal energy and absorbed solar energy at the top of atmosphere, is fundamental to understanding a planet or moon, as it has impacts on thermal structure, atmospheric circulation, and weather and climate patterns (1–3). The global radiant energy budgets have already been well determined for some planets and moons (4–12). The giant planets in our solar system can have large energy imbalances ( $\sim 80$  to  $150\%$ ) (2, 7, 10), caused by internal heat left over from formation. For terrestrial bodies (e.g., Earth, Titan, and Mars), the radiant energy budget is typically close to balanced, but seasonal and inter-annual imbalances are possible. Past studies have shown that for Earth a small energy imbalance is possible, around 0.2 to 0.4% of the emitted energy (4, 5). This small imbalance has significant impacts to the weather and climate of terrestrial bodies (4–6, 13). For Titan, our recent studies have shown an energy imbalance of  $\sim 2.9 \pm 0.8\%$  during the Cassini period, suggesting that Titan has a significantly dynamic energy budget (9, 11, 12, 14).

Compared with the numerous studies of the radiant energy budgets for these terrestrial bodies and gas giants, there are relatively few studies of the radiant energy budget for Mars. Previous studies of Mars' radiant energies mainly discussed limited areas (15–17), while other studies have relied on model results to estimate the energy budget (18, 19). Systematical studies of the global radiant energy budget are lacking, so a balanced global radiant energy budget is used in some previous work (18–21). Considering Mars' large axial obliquity and orbital eccentricity, we expect strong seasonal variations of radiant energies. Because of this, it is possible that Mars has an energy imbalance at the time scale of seasons, similar to what happens on Titan (11, 12). In addition, we cannot rule out a relatively long-term energy imbalance like that on Earth (5, 6, 13), which would significantly affect the climate on Mars.

In this study, we mainly use observations from the Thermal Emission Spectrometer onboard the Mars Global Surveyor (MGS/TES) from 1997 to 2005 (22–24), which are supplemented by the observations from other Mars missions (i.e., Mars Science Laboratory Curiosity Rover, and InSight Lander). Based on the Martian year designation from Clancy et al. (25), the observations used in this work span from Mars Year (MY) 24 to 28. During this time, there was a planet-encircling dust storm in 2001 (MY25). The evolution of this dust storm and its effects on surface and atmospheric conditions have been studied extensively in past work (26–30), but the storm's influence on the emitted energy has not been examined. The comparison of MY25 to years without a global dust storm allows us to better understand the impact of planet-encircling dust storms on the emitted energy. The MGS/TES observations also provide an excellent opportunity to examine the meridional, seasonal, and hemispheric averages of emitted power for the first time. Based on the measurements of Mars' emitted power and the estimates of the absorbed solar power, we further examine Mars' radiant energy budget especially at the time scale of seasons.

## Significance

The radiant energy budget is a fundamental metric for planets. Based on the observations from multiple missions, we provide a global picture of Mars' emitted power. Furthermore, we estimate the radiant energy budget of Mars, which suggests that there are energy imbalances at the time scale of Mars' seasons. Such energy imbalances provide a new perspective to understanding the generating mechanism of dust storms. Mars' radiant energy budget is assumed to be balanced at all time scales in current models and theories, but our analyses show that the energy budget is not balanced, at least at the time scale of Mars' seasons. Therefore, current theories and models should be revisited with the newly revealed energy characteristics.

Author affiliations: <sup>a</sup>Department of Earth and Atmospheric Sciences, University of Houston, Houston, TX 77004; <sup>b</sup>Department of Physics, University of Houston, Houston, TX 77004; <sup>c</sup>NASA Goddard Space Flight Center, Greenbelt, MD 20771; <sup>d</sup>Jet Propulsion Laboratory, California Institute of Technology, Pasadena, CA 91109; and <sup>e</sup>Lunar and Planetary Institute, Houston, TX 77058

Author contributions: L.L. designed research; E.C., L.L., and X.J. performed research; E.C., L.L., X.J., M.S., D.K., A.K., and G.M. contributed new reagents/analytic tools; E.C., L.L., X.J., M.S., D.K., A.K., and G.M. analyzed data; and E.C., L.L., and X.J. wrote the paper.

The authors declare no competing interest.

This article is a PNAS Direct Submission.

Copyright © 2022 the Author(s). Published by PNAS. This article is distributed under [Creative Commons Attribution-NonCommercial-NoDerivatives License 4.0 \(CC BY-NC-ND\)](https://creativecommons.org/licenses/by-nc-nd/4.0/).

<sup>1</sup>To whom correspondence may be addressed. Email: [ecreecy@central.uh.edu](mailto:ecreecy@central.uh.edu) or [llil7@central.uh.edu](mailto:llil7@central.uh.edu).

This article contains supporting information online at <http://www.pnas.org/lookup/suppl/doi:10.1073/pnas.2121084119/-DCSupplemental>.

Published May 3, 2022.

The theoretical methodology for computing the emitted energy has been applied in our previous work (8, 9, 11, 12, 14, 31) and is explained in *Materials and Methods*. The TES data processing is also discussed in *Materials and Methods* and briefly described here. The processed data are combined with the theoretical methodology to compute Mars' emitted power. In this study, we mainly focus on the seasonal variations of Mars' emitted power, but the temporal variations at other time scales (e.g., diurnal and interannual variations) are briefly discussed (*Materials and Methods*). *Materials and Methods* also includes error analysis for our computed emitted power. The time-varying solar flux, which plays a critical role in Mars' emitted power, is also provided in *Materials and Methods* (also see *SI Appendix, Fig. S1*).

We examine Mars' emitted energy using data acquired from MGS/TES from MY24 to MY28, which is publicly available on the Planetary Data System website (*Materials and Methods*). The high-quality data recorded by the TES thermal radiance bolometer covers all of MY25, MY26, MY27, and parts of MY24 (solar longitude [Ls] = 103 to 260°) and MY28 (Ls = 0 to 120°). In order to increase the spatial coverage in latitude and emission angle, the TES data are organized by MY according to the four seasons in the Northern Hemisphere (NH), with spring being Ls = 0 to 90°, summer Ls = 90 to 180°, autumn Ls = 180 to 270°, and winter Ls = 270 to 360°. There are still observational gaps in the domain of latitude and emission angle when organizing the data in each MY. Therefore, we average the data from each season across the five MYs to increase coverage. For example, we average all springs from MY24 to MY28 to get the springtime mean and do the same for summer and winter seasons. There was a planet-encircling dust storm that occurred during the autumn of MY25. In order to examine the impacts of this dust storm on the emitted radiance, we separate the autumn of MY25 from the autumns of MY24, MY26, and MY27.

The TES observations are mostly concentrated at 2 AM and 2 PM local times, so we first organize the TES data at 2 AM and 2 PM, respectively (*SI Appendix, Figs. S2–S7*). The effective wavelength range of the TES thermal bolometer is 5.3 to 100  $\mu\text{m}$  (24), but it does not cover the complete wavelength range contributing to Mars' thermal energy. Therefore, correction factors are applied for the incomplete spectral coverage (*Materials and Methods*). Most TES observations were conducted at emission angles less than 5°, so we can produce global maps in longitude and latitude at low emission angles (e.g., 0°) (*SI Appendix, Figs. S2 and S3*). For high emission angles, the TES data does not provide enough coverage to produce global maps in longitude and latitude. Therefore, the data are averaged in the direction of longitude to produce two-dimensional (2-D) data in the domain of latitude and emission angle. Then, the 2-D data are organized into the four seasons as discussed above. Even though we average the data over four seasons across the TES period, there are still observational gaps in the plane of latitude and emission angle (*SI Appendix, Figs. S4 and S5*), so we use linear interpolation and extrapolation to fill these gaps for the 2 AM/PM observations (*SI Appendix, Figs. S6 and S7*).

Based on the complete distribution of thermal radiance in the plane of latitude and emission angle, we can integrate the radiance over the direction of emission angle to get emitted power at different latitudes (see Eq. 1 in *Materials and Methods*). The TES measurements at 2 AM/PM (*SI Appendix, Figs. S8–S10*) are further combined with our investigations of the diurnal cycle of Mars' emitted power (*SI Appendix, Figs. S11 and S12*), which

are based on the observations from the Curiosity and InSight mission, to get the daily-mean emitted power. The uncertainties of meridional profiles of emitted power and their global/hemispheric averages are discussed in *Materials and Methods* (also see *SI Appendix, Figs. S13–S19*). After measuring the emitted power, we also estimate Mars' Bond albedo, the related absorbed solar power, and the radiant energy budget.

## Results

**Meridional Profiles of Emitted Power.** We first discuss the TES measurements of the meridional profiles of Mars' emitted power at 2 AM/PM in the four seasons (*SI Appendix, Fig. S8*), where the Northern autumn of MY25 has been excluded from the analyses. We find that the Mars' emitted powers are much stronger at 2 PM than at 2 AM for all four seasons, so the magnitude of the annual-mean emitted power is about five times stronger at 2 PM than at 2 AM. Due to Mars' thin atmosphere, the surface is the dominant contributor to the emitted power. In addition, the transport of solar heating from the dayside to nightside is not significant on Mars because of the lack of thick atmosphere and oceans. Therefore, the 2 PM (daytime) surface temperature is much hotter than the 2 AM (nighttime) surface temperature, which explains why the 2 AM emitted power is much weaker than the 2 PM emitted power.

For the 2 PM measurements in the NH, there is an increase in emitted power from Northern spring to summer, followed by a decrease from Northern summer to autumn and Northern autumn to winter, and finally an increase from Northern winter to spring. The seasonal variations are relatively strong for the seasonal transits from Northern summer to autumn and from Northern winter to spring in the NH. On the other hand, the seasonal variations are relatively weak for the seasonal transits from Northern spring to summer and from Northern autumn to winter. The emitted power of Mars is mainly affected by the thermal characteristics of the surface and atmosphere. The solar flux is the dominant factor in developing these thermal characteristics, helping us explain the seasonal variations of Mars' emitted power in the NH. The seasonal variations of solar flux (*SI Appendix, Fig. S1*) are relatively strong in the seasonal transits from Northern summer to autumn and Northern winter to spring and relatively weak for the seasonal transits from Northern spring to summer and Northern autumn to winter. This is consistent with the seasonal variations of emitted power in the NH.

For the 2 PM emitted power in the Southern Hemisphere (SH), there is an increase from Southern winter to spring, as well as Southern spring to summer, followed by a decrease from Southern summer to autumn, all of which are consistent with the seasonal variations of the solar flux in the SH (*SI Appendix, Fig. S1*). Furthermore, the seasonal variations of solar flux can help us explain the strength of the emitted power seasonal variations in the SH, in that the seasonal variations are relatively strong for the seasonal transits from Southern winter to spring and from Southern summer to autumn and relatively weak from Southern autumn to winter and from Southern spring to summer. It should be mentioned that the seasonal variation of emitted power from Southern autumn to winter is more complex. This variation changes sign between low latitudes and high latitudes in the SH, which cannot be explained by the seasonal variations of solar flux only. There are other factors (e.g., thermal characteristics of surface and dust storms of varying size) influencing the emitted power on Mars (32), which should be further explored.

We also find that the magnitude of seasonal variation for the 2 PM emitted power is stronger in the SH than in the NH (*SI Appendix, Fig. S8*). When Mars reaches its closest point from the Sun (i.e., perihelion at  $L_s = 251^\circ$ ), the global-average solar flux is at its maximum (*SI Appendix, Fig. S1B*). The season corresponding to perihelion is Southern spring, in which the sub-solar latitude is in the SH. Therefore, the maximal solar flux appears in the SH (*SI Appendix, Fig. S1A*), causing the seasonal variation of solar flux to be stronger in the SH than NH. The stronger seasonal variation of solar flux contributes to stronger seasonal variation of emitted power in the SH.

Now, we discuss the magnitude of seasonal variations of Mars' emitted power at 2 AM. Corresponding to the much smaller magnitudes of the 2 AM emitted power, the seasonal variations of the 2 AM emitted power are much smaller compared to these of the 2 PM emitted power. Even though the magnitudes of seasonal variations are different between the 2 PM and 2 AM emitted powers, the patterns of the seasonal variations are roughly the same between them.

Dust storms of smaller scale are common throughout a Martian year, but planet-encircling dust storms only occur during Mars' perihelion seasons ( $L_s = 180$  to  $360^\circ$ ). Dust storms greatly affect the dynamics of the Martian system, with changes to thermal structure, circulation, optical properties, and air-surface interaction (33–36). Dust suspended in the atmosphere creates an antigreenhouse effect, with dust absorbing over half the amount of incident solar radiation, causing atmospheric warming and surface cooling (19). At night, dust in the atmosphere creates a greenhouse effect, with dust effectively trapping outgoing surface radiation. The influence of global dust storms on atmospheric temperature has been well addressed in past studies (37), but little attention has been paid to the effects of dust storms on the emitted power.

In the Northern autumn of MY25 (i.e.,  $L_s = 185^\circ$ ), a local dust storm formed in Hellas Planitia and expanded to become planet-encircling by  $L_s = 193^\circ$  (27). We conduct a comparison of meridional profiles of emitted power and effective temperature during the Northern autumn of MY25 and “normal years” (i.e., MY24, MY26, and MY27 in which no global dust storm developed) (*SI Appendix, Fig. S9*). These normal years are averaged together during the Northern autumn season in order to compare to the MY25 autumn that includes a global dust storm. We first discuss the comparison of emitted power at 2 PM. In the relatively high latitudes of the two hemispheres (i.e.,  $\sim 45$  to  $90^\circ\text{N}$  and  $60$  to  $90^\circ\text{S}$ ), the emitted power in MY25 is slightly less compared to normal years. However, in the large latitudinal band from  $45^\circ\text{N}$  to  $60^\circ\text{S}$  the differences are more pronounced, with the 2 PM emitted power being significantly less in MY25 than in normal years. The global dust storm in MY25 first formed in the SH and had relatively larger dust coverage in the SH than in the NH, which can help explain the hemispheric asymmetry in the spatial distribution of the difference between MY25 and the normal years.

The global dust storm that occurred in the Northern autumn of MY25 clearly decreases the 2 PM emitted radiance compared to normal years, particularly near the equator and the low latitudes in the SH. Dust is a more effective absorber and reflector of solar radiation compared to the most abundant gas in Mars' atmosphere,  $\text{CO}_2$  (38). Under normal conditions, the Martian atmosphere is basically transparent to incoming solar irradiance, and the surface is the dominant emitter (19). During global dust storm conditions, dust suspended in the atmosphere significantly reflects and absorbs incident solar radiation (19), and the atmosphere becomes a primary emitter. While the

atmosphere is warmer during dust storm conditions compared to the atmosphere of normal years, it is still much cooler than the surface during normal years. This effect causes the decrease in 2 PM emitted power during MY25 autumn that is shown here.

Dust plays a different role in the emitted power at 2 AM. In nighttime, outgoing thermal radiation from the surface is significantly absorbed by dust in the atmosphere, with some radiation being reradiated back to the surface. The atmosphere during nighttime is warmer during dust storm conditions, and the combination of surface and atmospheric emitted energy contributes to a net emitted power increase in the autumn of MY25 compared to normal years. The observational characteristics of the effects of global dust storms on the emitted power, which are provided here, can be combined with a radiative-transfer model to better understand the roles of global dust storms in Mars' radiant energy budget.

**Hemispheric- and Global-Averaged Emitted Power.** Next, we discuss the hemispheric and global averages of emitted power in different seasons (*SI Appendix, Fig. S10 and Table S1*). We calculate the hemispheric and global averages in each season by integrating the meridional profiles of emitted power (*SI Appendix, Figs. S8 and S9*). The comparisons between the 2 PM and 2 AM analyses suggest significant diurnal variations in which the global-average, NH-average, and SH-average emitted powers at 2 PM are  $3.584 \pm 0.052$ ,  $3.618 \pm 0.049$ , and  $3.553 \pm 0.055$  times larger than the corresponding averages at 2 AM. There are also significant seasonal cycles for hemispheric and global averages at both 2 PM and 2 AM. The range of emitted power in the four seasons (i.e., the difference between the maximal emitted power and the minimal emitted power) can be used to represent the magnitude of the seasonal variations of emitted power (*SI Appendix, Table S1*). We find that the ranges of the 2 PM emitted power in the four seasons are  $53.1 \pm 7.0 \text{ Wm}^{-2}$ ,  $71.4 \pm 6.5 \text{ Wm}^{-2}$ , and  $160.0 \pm 6.3 \text{ Wm}^{-2}$  for the global average, NH average, and SH average, respectively. For the 2 AM emitted power, the ranges are  $14.8 \pm 1.28 \text{ Wm}^{-2}$ ,  $9.8 \pm 1.1 \text{ Wm}^{-2}$ , and  $33.0 \pm 1.36 \text{ Wm}^{-2}$  for the global average, NH average, and SH average, respectively. Dividing the ranges of emitted power in the four seasons over the annual-mean values, the percentages of seasonal variations of the 2 PM emitted power are  $25.9 \pm 3.4\%$ ,  $35.36 \pm 3.24\%$ , and  $76.6 \pm 3.1\%$  for the global average, NH average, and SH average, respectively. Likewise, for the 2 AM emitted power, the percentages are  $25.8 \pm 2.2\%$ ,  $17.6 \pm 2.0\%$ , and  $56.1 \pm 2.4\%$  for the global average, NH average, and SH average, respectively. For the hemispheric-average emitted power, the percentages are approximately two times stronger in the SH than in the NH for 2 PM and approximately three times stronger in the SH than in the NH for 2 AM. This means the magnitude of the seasonal cycle is stronger in the SH than in the NH, which can be explained by the stronger seasonal variations of solar flux in the SH than in the NH (*SI Appendix, Fig. S1*).

For the global-average emitted power, the percentages of seasonal variations are roughly the same between 2 PM and 2 AM ( $25.9 \pm 3.4\%$  and  $25.8 \pm 2.2\%$  for 2 PM and 2 AM, respectively). Mars' global-average emitted power is roughly one order of magnitude larger than the seasonal variation of Earth's emitted power ( $\sim 2.5$  to  $4\%$ ) (39, 40). There are two factors contributing to the large difference of seasonal cycles for the emitted power between Mars and Earth: 1) Mars has a much larger orbital eccentricity (0.0935) compared to Earth (0.0167) and 2) Earth has a significant atmosphere ( $\sim 1,000$  mbar) and oceans, while Mars has a very thin atmosphere ( $\sim 6$  mbar) and



no oceans. The large eccentricity of Mars' orbit makes the seasonal variation of solar flux much stronger than that on Earth. As the dominant factor influencing the emitted power, the strong seasonal variation of solar flux is the main reason why the seasonal variation of Mars' emitted power is strong as well. Earth's oceans and atmosphere can significantly store heat, unlike Mars which does not have similar heat storage. Earth's significant ability of heat storage and strong thermal inertial can help decrease its seasonal variations of temperature and emitted power.

Now we discuss the difference of hemispheric- and global-averaged emitted power between the MY25 NH autumn and other autumns (*SI Appendix*, Fig. S10). The global dust storm in MY25 modified the meridional profiles of emitted power at 2 PM/AM (*SI Appendix*, Fig. S9). Based on the meridional profiles of emitted power, we can compute the hemispheric and global averages. We find that the global dust storm in MY25 decreased the 2 PM emitted power by  $21.7 \pm 2.7\%$ ,  $23.3 \pm 2.6\%$ , and  $20.7 \pm 2.6\%$ , for the global average, NH average, and SH average, respectively. In contrast, the global dust storm increased the 2 AM emitted power by  $28.8 \pm 2.6\%$ ,  $33.2 \pm 2.2\%$ , and  $25.9 \pm 2.6\%$ , for the global average, NH average, and SH average, respectively.

**Resolving Mars' Diurnal Cycle of Emitted Power.** We further compare our results to previous studies that have estimated Mars' emitted power. Read et al. (19) estimated the emitted energy to be  $110 \text{ Wm}^{-2}$  under clear conditions, with an uncertainty of 6 to  $12 \text{ Wm}^{-2}$  for infrared fluxes. Haberle (18) estimated Mars' effective temperature to be  $\sim 208 \text{ K}$ , which correlates to an emitted power of  $106 \text{ Wm}^{-2}$ . The two studies both used numerical models to produce their results. Read et al. (19) used the European Mars Climate Database (version 5.0) (41) as well as the Nonlinear optimal Estimator for Multivariate spectral analysis (NEMESIS) (42) to estimate radiative fluxes. Haberle (18) used the Ames General Circulation Model to estimate Mars' effective temperature, and hence emitted power.

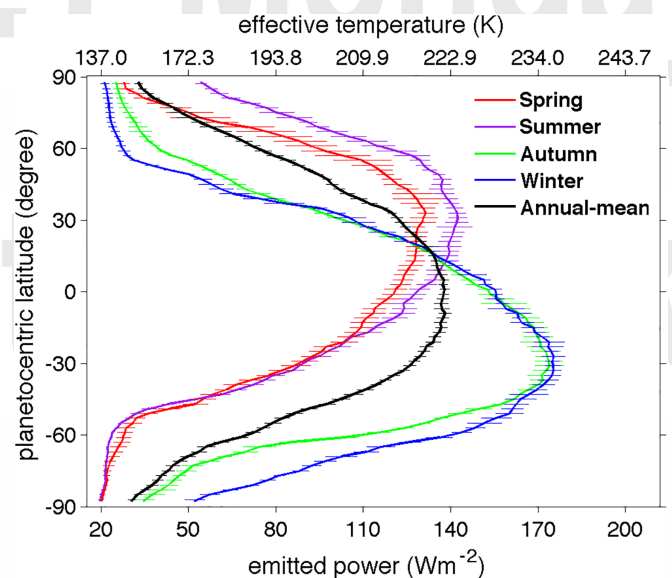
There are very few observational studies of Mars' emitted power. To our knowledge, the only estimate based on observations comes from Goody (20). Based on limited TES observations (one Martian year) and preliminary analysis, Goody (20) used the average of the measurements at two local times (2 PM and 2 AM) to estimate the emitted power of Mars, which generates a value of  $\sim 117 \text{ Wm}^{-2}$ . If Mars' thermal radiance follows a smooth diurnal cycle (i.e., sine function), then the average of the two points separated by one-half of the period (i.e., one-half of a Martian day) can represent the average of the complete cycle. However, the diurnal cycle of Mars' surface temperature, and hence emitted power, is more complicated and irregular (*Materials and Methods*). Therefore, the estimate using the average of the measurements over two local times may have a large uncertainty.

In order to better estimate the diurnal cycle of emitted power, we supplement with surface temperature data from the Mars Science Laboratory Curiosity Rover (43, 44) and InSight Lander (45). The diurnal cycle of surface temperature is used to estimate the diurnal cycle of emitted power (*SI Appendix*, Figs. S11 and S12). Based on the complete diurnal cycle of Mars' emitted power, we can get correction factors (*Materials and Methods*), which are defined as ratios between the daily-mean emitted power based on the complete diurnal cycle and the averaged emitted power over the two local times (2 PM and 2 AM) from the TES measurements. Such correction factors

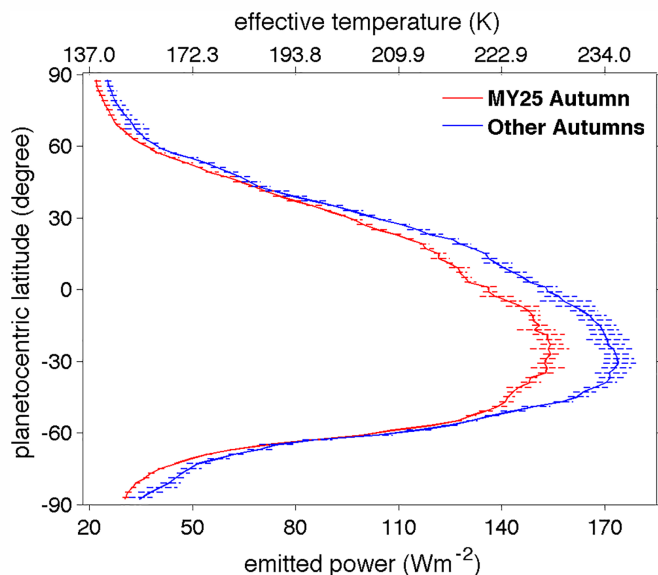
are applied to the averaged emitted power based on the MGS/TES measurements at 2 PM/AM (*SI Appendix*, Figs. S8–S10 and Table S1) to get the meridional profiles of Mars' daily-mean emitted power and their global/hemispheric averages. The uncertainties of these measurements, which includes the calibration errors, the uncertainty related to filling observational gaps, and the interannual variations of the seasonal analysis, are discussed in *Materials and Methods* (also see *SI Appendix*, Figs. S13–S19).

Fig. 1 shows the meridional profiles of daily-mean emitted power in the four seasons, which have the roughly same patterns as these in the 2 PM emitted power (*SI Appendix*, Fig. S8). The emitted power is much stronger at 2 PM than at 2 AM, meaning daytime thermal emission is dominant in Mars' daily-mean emitted power. Therefore, Mars' daily-mean emitted power in different seasons follows basically the same structures as those of the 2 PM emitted power. The global dust storm in MY25 decreased the emitted power at 2 PM but increased the emitted power at 2 AM (*SI Appendix*, Fig. S9). Fig. 2 shows the comparison of meridional profiles of daily-mean emitted power between MY25 autumn and other autumns, which suggests the global dust storm decreased Mars' emitted power overall.

The daily-mean emitted powers in different seasons are averaged over time and space to get the annual-mean emitted powers at hemispheric and global scales, which is shown in Fig. 3 (also see *SI Appendix*, Table S2). We find the annual-mean global-average emitted power to be  $111.7 \pm 2.4 \text{ Wm}^{-2}$ , which is consistent with previous estimates ( $106$  to  $117 \text{ Wm}^{-2}$ ) (18–20, 46). Our measurements of emitted power can be used to refine the estimates of the Bond albedo. The terrestrial bodies in our solar system (e.g., Earth and Titan) generally have a roughly balanced annual-mean radiant energy budget (4, 9) even though a small energy imbalance ( $<3\%$  of the emitted energy) is possible (5, 11). Here, we assume that Mars also has a basically balanced annual-mean energy budget. The annual-mean global-average solar flux at Mars is  $\sim 147.24 \text{ Wm}^{-2}$  (*SI Appendix*, Fig. S1). Balancing the absorbed solar power [i.e.,  $147.24 \times (1 - A)$ , where  $A$  is the Bond albedo of Mars] by our



**Fig. 1.** Meridional profiles of Mars' emitted power in four seasons. The results presented here are based on the TES daytime (2 PM) and nighttime (2 AM) analyses (*SI Appendix*, Fig. S8) and the complete diurnal cycle of Mars' emitted power (*SI Appendix*, Figs. S11 and S12).



**Fig. 2.** Comparison of meridional profiles of Mars' emitted power between MY25 autumn and other autumns. The results presented here are based on the TES daytime (2 PM) and nighttime (2 AM) analyses of the global dust storm in MY25 autumn (*SI Appendix, Fig. S9*) and the complete diurnal cycle of Mars' emitted power (*SI Appendix, Figs. S11 and S12*).

estimated thermal power ( $111.7 \pm 2.4 \text{ Wm}^{-2}$ ), we have the Bond albedo  $\sim 0.241 \pm 0.016$ . This estimate is consistent with the results from some previous studies (e.g., 0.23 to 0.26) (18, 19, 47), even though other investigations suggest different values of Bond albedo (48, 49). The uncertainty in the refinement ( $\pm 0.016$ ) of Mars' Bond albedo corresponds to  $\sim 2.4 \text{ Wm}^{-2}$  uncertainty in the absorbed solar power, which is  $\sim 2.1\%$  of the emitted power. That means our refinement of Mars' Bond albedo is trustable except that Mars has a much larger energy imbalance than these discovered on Earth and Titan ( $<3\%$  of the emitted power) (5, 11).

**Estimations of the Seasonal Absorbed Solar Power and Energy Budget.** Based on the estimated Bond albedo, we can estimate the absorbed solar powers at the time scale of seasons. The Bond albedo of planets and moons are generally stable at

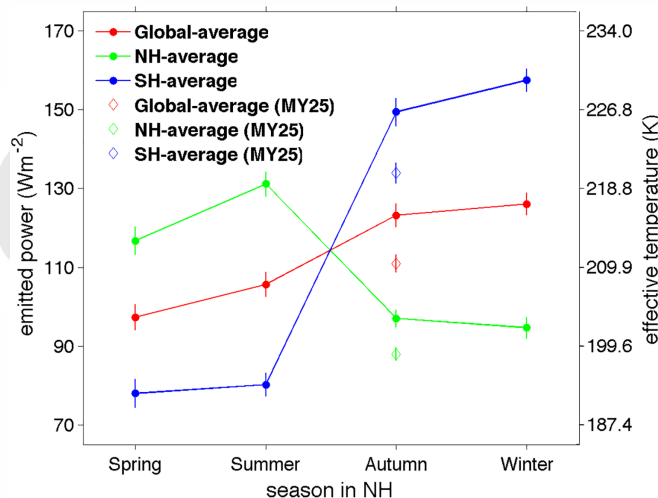


**Fig. 3.** Global and hemispheric averages of Mars' emitted power in four seasons (including MY25 autumn). The results presented here are based on the meridional profiles of Mars' emitted power (Figs. 1 and 2).

the time scale of seasons (e.g., refs. 5, 10, and 11). Therefore, we assume that Mars' Bond albedo does not change with seasons, and we consider regular atmospheric conditions without the global dust storms. Considering the asymmetry of Mars' albedo between the two hemispheres (50–53), we use the global albedo (*SI Appendix, Fig. S20*) retrieved from the TES visible observations (51) to get the hemispheric-average albedos (*Materials and Methods*). Then, we can use the solar flux at Mars (*SI Appendix, Fig. S1*) to compute the global and hemispheric absorbed solar powers.

Fig. 4 suggests that the global-average absorbed solar powers are  $96.8 \text{ Wm}^{-2}$ ,  $103.8 \text{ Wm}^{-2}$ ,  $130.5 \text{ Wm}^{-2}$ , and  $122.4 \text{ Wm}^{-2}$  for Northern spring, summer, autumn, and winter, respectively. The global-average emitted powers are  $97.3 \pm 2.7 \text{ Wm}^{-2}$ ,  $105.7 \pm 2.3 \text{ Wm}^{-2}$ ,  $123.2 \pm 2.4 \text{ Wm}^{-2}$ , and  $126.1 \pm 2.3 \text{ Wm}^{-2}$  for Northern spring, summer, autumn, and winter, respectively (*SI Appendix, Table S2*). The comparison between the global-average emitted thermal power and absorbed solar power suggests that the difference between the two energy components is much larger in Northern autumn ( $\sim 7.3 \text{ Wm}^{-2}$ ) compared to other seasons (0.5 to  $3.7 \text{ Wm}^{-2}$ ). In addition, Northern autumn (Southern spring) is the only season with energy excess (i.e., the absorbed solar energy is larger than the emitted thermal energy) at a global scale.

Fig. 4 also shows the comparison of hemispheric-average values between emitted power and absorbed solar power. We have the NH-average absorbed solar powers for the four seasons as  $119.1 \text{ Wm}^{-2}$ ,  $127.3 \text{ Wm}^{-2}$ ,  $91.8 \text{ Wm}^{-2}$ , and  $85.9 \text{ Wm}^{-2}$  for Northern spring, summer, autumn, and winter, respectively. Correspondingly, we have the SH-average absorbed solar powers for the four seasons in the normal Martian years as  $72.6 \text{ Wm}^{-2}$ ,  $78.4 \text{ Wm}^{-2}$ ,  $172.2 \text{ Wm}^{-2}$ , and  $161.9 \text{ Wm}^{-2}$  for Northern spring, summer, autumn, and winter, respectively. The hemispheric-average emitted powers in the four seasons are provided already (*SI Appendix, Table S2*). For the NH, Fig. 4 suggests that the absorbed solar fluxes are larger than the emitted power in Northern spring but smaller than the emitted power in other seasons. For the SH-average analysis, the absorbed solar power is larger than the emitted power in Northern autumn and winter but smaller than the emitted power in Northern spring and summer. In particular, the SH-average energy excess (the absorbed solar power – the emitted power) can reach  $\sim 22.8 \text{ Wm}^{-2}$ , which is much larger than all energy excesses in other

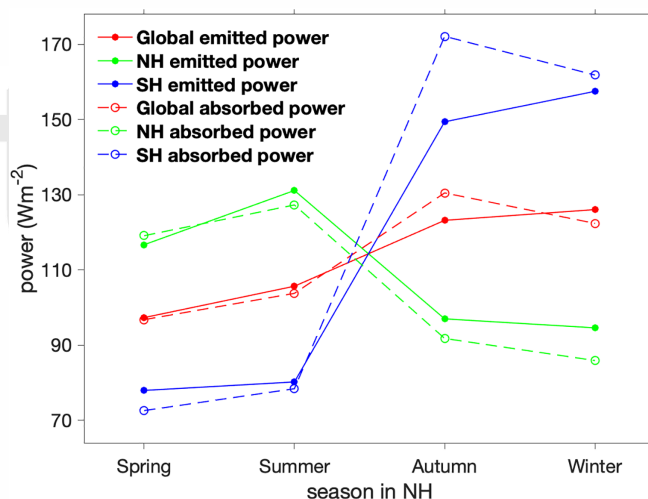


**Fig. 4.** Comparison between the emitted thermal power and absorbed solar power of Mars. Both global and hemispheric averages are shown.

seasons for the two hemispheres. The energy excess in Northern autumn (i.e., Southern spring) for the SH ( $\sim 22.8 \text{ Wm}^{-2}$ ) is  $\sim 15.3\%$  of the emitted energy ( $\sim 149.4 \text{ Wm}^{-2}$ ). In addition, the energy excess still exists in Northern winter (i.e., Southern summer) in the SH even though the magnitude decreased.

It should be mentioned that the above analysis is based on the TES albedo with a Lambert-surface assumption (51). Precise measurements of Mars' Bond albedo require perfect coverages of spatial domain, wavelength, and viewing angle, which are still limited or lacking in current studies of Mars' albedo. It is possible to combine observations from different missions to provide much better measurements of Mars' albedo and its variabilities, which will provide even better information on the seasonal energy imbalance on Mars.

The energy excesses that happened in the SH during Northern autumn and winter (i.e., Southern spring and summer) can be one of the generating mechanisms of the dust storms in this region. The energy excess warms Mars' surface (SI Appendix, Fig. S21) and the atmosphere near the surface, which hence increases the vertical temperature contrast for Mars' atmospheric boundary layer. The increased temperature contrast further helps develop convective instability of the boundary atmosphere and prompt dust storm formation. Further theoretical and numerical studies are needed to carefully examine the roles of the energy excess in atmospheric dynamics and the development of dust storms. Furthermore, dust storms, including the global dust storms, which modify the emitted thermal power (Fig. 2) and the absorbed solar power by changing Mars' Bond albedo, could work to reequilibrate the radiant energy budget.

## Discussion

In this study we present our results examining Mars' emitted energy based on the data from multiple missions, which are further used to estimate Mars' radiant energy budget. The analysis based on the long-term MGS/TES observations suggests that Mars' daytime (2 PM) and nighttime (2 AM) emitted power displays strong seasonal variations in both hemispheres. The magnitudes of seasonal cycles of the hemispheric-average emitted power are approximately two and three times stronger in the SH than in the NH for the 2 PM and 2 AM emitted powers, respectively. The magnitude of seasonal variations for the global average are  $25.9 \pm 3.4\%$  and  $25.8 \pm 2.2\%$  for the 2 PM and 2 AM analyses, respectively, which are roughly one order magnitude larger than the seasonal variations of Earth's emitted power ( $\sim 2.5$  to  $4\%$ ) (39, 40). We also explore the role of the MY25 planet-encircling dust storm in Mars' emitted power. We found that the global dust storm in MY25 decreased the global-average emitted power at 2 PM but increased the global-average emitted power at 2 AM. This difference between 2 AM/PM is largely caused by dust suspended in the atmosphere.

The comparisons between 2 AM/PM measurements also suggest a significant diurnal cycle of Mars' emitted power. The strong diurnal cycle is caused in part by lack of liquid oceans and large atmosphere, both of which can help transport energy and decrease differences of temperature and emitted power between dayside and nightside. The surface temperature data from the Curiosity Rover and InSight Lander are used to help estimate the daily-mean emitted power, which is then used to calculate an annual-mean global-average emitted power ( $111.7 \pm 2.4 \text{ Wm}^{-2}$ ). Additionally, our estimates of the absorbed solar power suggest that there are significant energy imbalances at

different seasons of the two hemispheres, which are mainly caused by the dynamic nature of the seasonal variations of Mars' emitted energy and absorbed solar power. In particular, we find there is an energy imbalance  $\sim 15.3\%$  of the emitted power for Northern autumn in the SH, which probably plays an important role in developing dust storms on Mars. Numerical models have become very advanced in their abilities to simulate circulation, weather and climate patterns, and radiative transfer on Mars (54–57). Combining our observational characteristics of Mars' radiant energy budget with these numerical models can help to further improve our understanding of the climate and atmosphere of the red planet.

## Materials and Methods

**Theoretical Methodology.** The radiant energy budget of a planet is determined by two radiant energies: the emitted thermal energy from the planet and the solar energy absorbed by the planet. Radiant energies over a unit area are defined as radiant powers. The theoretical methodology for computing emitted power has been described in past studies (2, 3) and used in our previous work of studying the radiant energy budget of planets and moons (8, 11, 12, 14). Here, we describe the basic concepts of computing the emitted power, and therefore effective temperature.

It is generally valid to assume that the emitted energy depends only on the emission angle and not the azimuth angle (2, 3). The emission angle is defined as the angle between the observer (i.e., MGS/TES) and the surface normal. The emitted energy per unit time over a defined unit area is defined as the emitted power. Therefore, the emitted power, or  $P_{\text{emit}}$ , is given in the format of spectral flux, or  $I_\nu$ :

$$P_{\text{emit}} = 2\pi \int_{\nu_1}^{\nu_2} \int_0^{\pi/2} I_\nu(\delta) \cos\delta \sin\delta d\delta d\nu \approx 2\pi \sum_j I(\delta_j) \cos\delta_j \sin\delta_j \Delta\delta, \quad [1]$$

where  $\nu$  is the wavenumber and  $\delta$  is the emission angle (58, 59). The wavenumber integrated radiance is given by  $I(\delta_j)$  in Eq. 1. Given Eq. 1, we can calculate the emitted power,  $P_{\text{emit}}$ , using observed radiance  $I(\delta_j)$  at discrete emission angles. From this calculation of emitted power, we can estimate the effective temperature (i.e., the temperature of a blackbody that would emit the same amount of emitted power) in the following equation, where  $\sigma$  is the Stefan-Boltzmann constant and  $T_{\text{eff}}$  is the effective temperature:

$$P_{\text{emit}} = \sigma T_{\text{eff}}^4. \quad [2]$$

After getting the emitted power at each latitude, we have the global-average emitted power (8, 60) as

$$\bar{P} = \frac{1}{2(1 - 2\epsilon/3)} \sum_{i=1}^N (1 - 2\epsilon \sin^2\phi_i) P(\phi_i) \cos\phi_i \Delta\phi = \sum_{i=1}^N c_i P(\phi_i), \quad [3]$$

where  $\epsilon$  is the oblateness of Mars ( $\sim (3396.2 - 3376.2)/3396.2 \sim 0.0059$ ),  $\phi$  is latitude, and  $P(\phi_i)$  is the emitted power at the latitude  $\phi_i$ . The index  $N$  is the number of latitude bands from pole to pole. The coefficient  $c_i$  is represented by  $c_i = [(1 - 2\epsilon \sin^2\phi_i) \cos\phi_i \Delta\phi] / [2(1 - 2\epsilon/3)]$ . Likewise, we can use Eq. 3 to get the hemispheric-average emitted power for the NH and the SH by constraining the latitude bands to the NH and SH, respectively.

For the other radiant energy component, the absorbed solar power, the Bond albedo is a key parameter. Generally, the Bond albedo can be measured by observed reflected solar radiance at different phase angles. The total solar flux at a planet is determined once the distance between the planet and the Sun is known (see the next section). Then, the absorbed solar power can be computed with the measured Bond albedo and the total solar flux. Finally, we can determine the radiant energy budget with the emitted thermal power and the absorbed solar power. The precise measurements of Mars' Bond albedo, which should involve observations of reflected solar radiance with phase angle varying from  $0^\circ$  to  $180^\circ$ , are still lacking. In this study, we estimate Mars' Bond albedo by assuming a basic balance between the annual-mean emitted thermal power and absorbed solar power. Then, the estimated Bond albedo is used to investigate the radiant energy budgets at the time scale of Martian seasons, which probably play an important role in developing dust storms on Mars.



**Solar Flux on Mars.** The emitted power of Mars is mainly affected by the thermal characteristics of surface and atmosphere. The solar flux is the dominant factor developing the thermal characteristics of Mars' surface and atmosphere. In addition, the solar flux can help us determine the absorbed solar power with Bond albedo. Therefore, it is necessary to discuss the spatiotemporal variations of solar flux on Mars. There are two dominant factors that influence the distribution of solar flux on Mars: 1) Mars' axial tilt of  $25.19^\circ$  and 2) the eccentric orbital path Mars follows around the Sun (eccentricity  $\sim 0.0935$ ). Mars' relatively large axial tilt angle significantly impacts how incident solar radiation is distributed across latitudes, while the large orbital eccentricity affects the Mars-Sun distance and hence the total solar flux. Mars reaches its furthest point from the Sun ( $\sim 1.666$  AU), or aphelion, during Northern spring ( $L_s = 71^\circ$ ) and closest point to the Sun ( $\sim 1.381$  AU), or perihelion, during Northern autumn ( $L_s = 251^\circ$ ). Considering the two effects (i.e., obliquity and eccentricity), we can calculate the solar flux in the plane of latitude and solar longitude (i.e., season) (*SI Appendix, Fig. S1*). The global-average solar flux (*SI Appendix, Fig. S1B*) increases  $\sim 45.4\%$  from  $\sim 123.06 \text{ Wm}^{-2}$  at aphelion to  $\sim 178.94 \text{ Wm}^{-2}$  at perihelion. The changes of solar flux at some latitudes can be even more pronounced.

**TES Data Processing.** Our analysis of Mars' emitted power is mainly based on the data recorded at two local times (2 PM/AM) by the TES onboard the MGS. In addition, the observations of surface temperature from other Mars missions (see *Diurnal Cycles of Surface Temperature and Daily-Mean Emitted Power*) are used to address the diurnal cycle of Mars' emitted power. For the MGS/TES (24), there are three subinstruments: 1) a Michelson interferometer/spectrometer, which takes measurements in the spectral range of  $200$  to  $1,600 \text{ cm}^{-1}$  ( $6$  to  $50 \text{ }\mu\text{m}$ ) with a sampling of either  $5$  or  $10 \text{ cm}^{-1}$ , 2), a bore-sighted bolometric thermal radiance spectrometer ( $5.3$  to  $100 \text{ }\mu\text{m}$ ), and 3) a solar reflectance spectrometer ( $0.3$  to  $2.7 \text{ }\mu\text{m}$ ). Here, we use the data recorded by the bolometric thermal radiance spectrometer because it has a wide wavelength coverage for the thermal radiance from Mars. There are six detectors in the bolometric thermal spectrometer. The six detectors have quasi-simultaneously observational time and their observational locations are generally very close. Our tests suggest that there are significant differences among the thermal radiances recorded by the six detectors only for very few observations. When averaging over seasons, we did not find any significant difference for the season-average analysis among different detectors. Therefore, we select the observations recorded by the third detector in the bolometric thermal spectrometer to conduct our seasonal analysis of Mars' emitted power. The orbits of the MGS have a relatively low altitude ( $\sim 378 \text{ km}$ ) and the detectors in the three TES subinstruments have a field of view of  $8.3 \text{ mrad}$ . Therefore, the TES observations have a spatial resolution of  $\sim 6 \text{ km}$ . The MGS was in a near-polar orbit that was roughly around the same local times (2 AM or 2 PM) for most latitudes. The high-quality data recorded by the TES bolometric thermal radiance spectrometer covers MY25, MY26, MY27, and parts of MY24 ( $L_s = 103$  to  $260^\circ$ ) and MY28 ( $L_s = 0$  to  $120^\circ$ ).

In order to compute the emitted power using the theoretical framework discussed above, we first must process the TES dataset. We download the data recorded by the TES thermal bolometer from the Planetary Data System mentioned above. The TES observations were mainly conducted at 2 AM and 2 PM, respectively, so we organize the data into two groups (2 PM and 2 AM). Through this organization, we can examine Mars' emitted power in both daytime and nighttime. We then process the data with  $1^\circ$  resolution in latitude, longitude, and emission angle and  $10^\circ$  resolution in solar longitude (i.e.,  $L_s$ ). Most TES observations were conducted at emission angle less than  $5^\circ$ . Therefore, we can produce global maps with high spatial resolution at low emission angles (e.g.,  $0^\circ$ ) (*SI Appendix, Figs. S2 and S3*).

*SI Appendix, Fig. S2* shows that the thermal radiance at emission angle  $0^\circ$  is much stronger at 2 PM (panels in left column) than at 2 AM (panels in right column). As we discussed in the main text, the lack of oceans and significant atmosphere is the main reason why the emitted power is so different between daytime and nighttime. The spatial patterns of thermal radiance are also different between the 2 PM and 2 AM maps. The thermal radiance is larger in highlands than lowlands in the 2 PM global maps but the opposite happens in the 2 AM global maps. The main reason for this difference is the thermal inertia and albedo of the various terrains. During the night (i.e., the 2 AM observations), the pattern is dominated by thermal inertia. For the daytime pattern (i.e., the 2 PM observations), albedo is also important to consider in addition to thermal inertia.

*SI Appendix, Fig. S2* also displays significant seasonal variations of Mars' thermal radiance at  $0^\circ$  emission angle. For both 2 PM and 2 AM maps, the latitudinal band of maximal thermal radiance stays relatively constant for both Northern spring and summer. After that, the latitudinal band of maximal thermal radiance continuously moves southward from Northern summer to winter corresponding to the similar moving of subsolar latitude. Finally, the latitude band of maximal thermal radiance moves northward from Northern winter to spring when the subsolar latitude begins to move northward again. In addition to the meridional shifts of maximal thermal radiance, the magnitude of thermal radiance also displays strong seasonal variations. *SI Appendix, Fig. S2* shows the magnitudes of the emitted power in Northern spring and summer are weaker than those in Northern autumn and winter for both 2 PM and 2 AM maps. This can be explained by Northern spring and summer occurring around aphelion ( $L_s = 71^\circ$ ), with the longest Mars-Sun distance and weakest solar flux. Comparatively, Northern autumn and winter occur around perihelion ( $L_s = 251^\circ$ ) with the shortest Mars-Sun distance strongest solar flux (*SI Appendix, Fig. S1*).

*SI Appendix, Fig. S3* shows the comparison of global maps between MY25 autumn (with a global dust storm) and other autumns. The thermal radiance is smaller in MY25 autumn compared to other autumns for the 2 PM global maps, but the thermal radiance is larger in MY25 autumn compared to other autumns for the 2 AM global maps. As discussed in the main text, the significant dust suspended in atmosphere, which is related to the global dust storm, helps decrease the daytime surface temperature and emitted power by blocking the solar flux. At night, dust suspended in atmosphere helps trap thermal radiance from surface, warming the surface temperature and emitted power.

*SI Appendix, Figs. S2 and S3* show the global maps of Mars' thermal radiance at  $0^\circ$  emission angle. At higher emission angles, there is much worse spatial coverage, which makes it impossible to make global maps of Mars' thermal radiance at high spatial resolutions (e.g.,  $1^\circ$  resolution in both longitude and latitude). Therefore, we reorganize the data with  $30^\circ$  resolution in longitude,  $2^\circ$  in latitude,  $2^\circ$  in emission angle, and  $90^\circ$  in solar longitude. The resolution for longitude is poor because we are mostly concerned with the meridional distribution. The temporal resolution ( $90^\circ$  solar longitude) is chosen for examining the seasonal variations. In this study, we use the seasons in the NH (i.e.,  $L_s = 0$  to  $90^\circ$  Spring,  $L_s = 90$  to  $180^\circ$  Summer,  $L_s = 180$  to  $270^\circ$  Autumn, and  $L_s = 270$  to  $360^\circ$  Winter). Since the Northern summer of MY28 is not fully covered by the observations, it is not included in the analyses. The TES data are also organized into 2 PM and 2 AM observations, respectively, so we can examine Mars' emitted power in both daytime and nighttime.

We average the four-dimensional matrix (latitude  $\times$  longitude  $\times$  emission angle  $\times$  solar longitude) over longitude to get a three-dimensional matrix (latitude  $\times$  emission angle  $\times$  solar longitude). Even after using the relatively coarse resolutions, the coverage is still limited in the plane of latitude and emission angle. There are significant observational gaps in the domain of latitude and emission angle when organizing the data in each MY. Therefore, we average the data from each season across the five MYs to increase coverage. For example, we average all springs from MY24 to MY28 to get the springtime mean and do the same for summer and winter seasons. There was a planet-encircling dust storm that occurred in 2001, which is the autumn of MY25. In order to examine the impacts of this dust storm on the emitted power, we separate the autumn of MY25 from the autumns of "normal years" without a global dust storm (i.e., MY 24, 26, and 27). The autumns of normal years are averaged together and then compared to the autumn of MY25. Then, we have the processed data for each season (*SI Appendix, Fig. S4*) and the comparison between normal-year autumns and MY25 autumn (*SI Appendix, Fig. S5*).

The processed data in the plane of latitude and emission angle have good coverage at most latitudes for the four seasons, and we use linear interpolation/extrapolation to fill gaps in emission angle for these latitudes with relatively poor coverage of emission angle. Some regions, especially near the polar region, have significant observational gaps in the direction of latitude. To address this, we also use linear interpolation/extrapolation in the direction of latitude to fill the gaps. After the process of filling observational gaps, we now have Mars' emitted radiance with complete coverage in the domain of latitude and emission angle for four Mars seasons (*SI Appendix, Fig. S6*). Again, the autumn of MY25 is separated from that of normal years (*SI Appendix, Fig. S7*).

Based on the 2-D data shown in *SI Appendix, Figs. S6 and S7*, we integrate the data in the direction of emission angle to get the meridional profile of

emitted power in the four seasons for both 2 PM and 2 AM observations (*SI Appendix, Fig. S8*). We again separate the autumn of MY25 from normal years to compare the meridional profile of emitted profile (*SI Appendix, Fig. S9*). By integrating the data in the direction of latitude, we then have the global and hemispheric averages of emitted power (*SI Appendix, Fig. S10*).

**Correction Factors for Incomplete Wavelength Coverage of TES Observations.** The effective wavelength range of the TES thermal bolometer, which can be estimated by the sharp slope of the response level (24), is  $\sim 5.3$  to  $100\ \mu\text{m}$ . Such a wavelength range does not cover the complete wavelength for Mars' total thermal radiance. Therefore, correction factors are needed for computing Mars' emitted power at 2 PM and 2 AM. *SI Appendix, Table S1* shows that the global-average effective temperatures are  $\sim 246\ \text{K}$  and  $\sim 179\ \text{K}$  for 2 PM and 2 AM, respectively. Assuming a blackbody with a temperature  $246\ \text{K}$ , we compute the blackbody spectrum from  $0\ \mu\text{m}$  to  $1,000\ \mu\text{m}$ . The ratio of integrated radiance between the total wavelength range ( $0$  to  $1,000\ \mu\text{m}$ ) and the TES wavelength range ( $5.3$  to  $100\ \mu\text{m}$ ), which has a value  $1.012$ , is used for the correction factor for the TES measurements at 2 PM. For the measurements of emitted power at 2 AM, we did the same except for assuming the blackbody having a temperature  $179\ \text{K}$ . This method generates a correction factor  $1.020$  for the 2 AM measurements.

**Diurnal Cycles of Surface Temperature and Daily-Mean Emitted Power.** The MGS/TES observations are mainly concentrated at 2 PM and 2 AM, meaning the complete diurnal cycle of Mars' emitted power cannot be addressed. Here, we use the temperature data from the Mars Science Laboratory Curiosity Rover (43, 44) and InSight Lander (45) to explore the diurnal cycle of surface temperature and hence emitted power for Mars. It should be mentioned that there are other in situ measurements of Mars' surface temperature (e.g., Phoenix and Mars Exploration Rover Spirit and Opportunity), but their coverage of diurnal cycle is not as good. Therefore, these measurements are not included in our analysis of the diurnal cycle of Mars' surface temperature.

Data obtained from Curiosity spans all four seasons, covering the first 2,500 sols on Mars, while InSight data only covers Northern spring, summer, and winter, spanning 312 sols in total. The location of the Curiosity Rover is  $\sim 4.5^\circ\text{S}$  latitude, while the InSight Lander is  $\sim 4.5^\circ\text{N}$  latitude. Both Curiosity and InSight have good diurnal coverage, so it is possible to find the 24-h average of surface temperature and hence emitted power in each season.

For processing the Curiosity and InSight data, the first step is to convert the surface temperature to the emitted power. We approximate Mars as a blackbody, so we can use the Stefan-Boltzmann equation (Eq. 2) to compute its emitted power. The main idea is to calculate the daily-mean emitted power at the surface and find the ratio between the daily-mean and 2 AM/PM average given by MGS/TES observations then use this ratio as a correction factor that is applied to the MGS/TES dataset. After calculating the emitted power at the surface based on the Stefan-Boltzmann equation (Eq. 2), we then separate the data by season. For Curiosity, all the observations used occur at evenly spaced one-hour intervals (i.e.,  $0, 1, 2, \dots, 23$ ). To calculate the 24-h cycle for Curiosity observations, we average all data points for each individual hour point within each season. For example, we take all the 0-h points in the Northern spring season ( $L_s = 0$  to  $90^\circ$ ) and average them together to obtain the 0-h average for the Northern spring season. We do this for both the surface temperature and calculated emitted power. The diurnal cycle of both surface temperature and emitted power for Curiosity observations can be seen in *SI Appendix, Fig. S11*. For InSight, the observations are not separated by exact 1-h intervals. Therefore, in order to find the 24-h cycle, we collect all points that fall within a 1-h range for each season (i.e.,  $0$  to  $1$ ,  $1$  to  $2$ ,  $\dots$ ,  $23$  to  $24$ ) and then calculate the average of those points. For example, we collect all points that fall between  $0$  and  $1\ \text{h}$  during the Northern spring season and average them together to find the 0-h Northern spring average. This is done again for both surface temperature and calculated emitted power. The diurnal cycle of both surface temperature and emitted power for InSight observations can be seen in *SI Appendix, Fig. S12*.

Based on *SI Appendix, Figs. S11 and S12*, we can get the ratios between the daily-mean emitted power based on the complete diurnal cycle and the averaged emitted power over the two local times (2 PM and 2 AM). We take the ratios as the correction factors for the averaged emitted power based on the TES measurements at 2 PM and 2 AM (*SI Appendix, Fig. S8*). Using Curiosity data, we have the correction factors of  $0.821$ ,  $0.841$ ,  $0.863$ , and  $0.823$  for Northern

spring, summer, autumn, and winter, respectively, using Curiosity data. The correction factors for InSight are  $0.850$ ,  $0.878$ , and  $0.870$  for Northern spring, summer, and winter, respectively. These correction factors are interpolated/extrapolated to all latitudes and four seasons. Then, we apply the factors to the meridional profile of Mars' emitted power from TES measurements (*SI Appendix, Fig. S8*) to get the meridional profiles of the daily-mean emitted power in four seasons (Fig. 1). We also conduct the comparison of the daily-mean emitted power between MY25 autumn and the normal autumns (Fig. 2). Finally, the meridional profiles of daily-mean emitted power (Figs. 1 and 2) are averaged to global/hemispheric averages, which are shown in Fig. 3. The global/hemispheric values of Mars' daily-mean emitted power are shown in *SI Appendix, Table S2*.

**Interannual Variations of Mars' Thermal Radiance.** In order to increase the coverage of TES observations in the 2-D domain of emission angle and latitude, we average the data from each season across the five Martian years. Such processed data cannot be used to investigate the interannual variations of Mars' emitted power. As we discussed above (*SI Appendix, Figs. S2 and S3*), the TES data have the relatively good spatial coverage at  $0^\circ$  emission angle. Here, we discuss the interannual variations of Mars' thermal radiance at  $0^\circ$  emission angle. *SI Appendix, Fig. S13* shows that the meridional profiles of Mars' thermal radiance at  $0^\circ$  emission angle in four seasons for different Martian years, which suggests that the interannual variations are not significant for most latitudes, excluding the effects of global-scale dust storms.

Based on *SI Appendix, Fig. S13*, we compute the ratio between the SD and mean of the emitted power in different Martian years (*SI Appendix, Fig. S14*). We find that the ratio is less than  $10\%$  for most latitudes. If we assume that the SD of Mars' thermal radiance is the same between  $0^\circ$  emission angle and other emission angles, we can use the observations at  $0^\circ$  emission angle (*SI Appendix, Fig. S13*) to estimate the SD of Mars' emitted power in different Martian years. The comparison between such SD and the errors related to filling observational gaps (see the next section) shows that they are comparable at most latitudes. Therefore, the interannual variations of Mars' thermal radiance do not significantly affect our discussions of the diurnal and seasonal variations of Mars' emitted power. However, we include the SD related to the interannual variations of Mars' thermal radiance into our analysis of the uncertainties (see the section below).

Based on the meridional profiles of Mars' thermal radiance at  $0^\circ$  emission angle, we also examine the interannual variations of the global-average thermal radiance. Even though the SD of Mars' thermal radiance at  $0^\circ$  emission angle in different Martian years can reach  $10\%$  of the mean value at some latitudes (*SI Appendix, Fig. S14*), the SD of the global-average thermal radiance in different Martian years is relatively small. *SI Appendix, Fig. S15* shows that the ratio between the SD and mean of the global-average thermal radiance is less than  $3\%$ .

**Error Analysis for Mars' Emitted Power.** There are two uncertainty sources we consider when calculating the emitted energy: 1) the uncertainty related to the calibration of the MGS/TES data and 2) the uncertainty related to filling observational gaps. In this study, we focus on the seasonal analysis of Mars' emitted power and such an analysis is based on the processed data averaging the TES observations over each season across the five Martian years (MY 24 to 28). Therefore, the interannual variations of Mars' thermal radiance, which are discussed in the above section (*SI Appendix, Figs. S13–S15*), should be also included in the estimate of the uncertainty of Mars' seasonal emitted power.

We first discuss the uncertainty related to the TES data calibration. The calibration of the dataset is publicly available (24). The basic idea of calibrating the data recorded by the TES thermal bolometer is to use observations of deep space acquired away from Mars (24). The derived  $1\text{-}\sigma$  variation in the zero-level radiance is  $\sim 3.75 \times 10^{-2}\ \text{Wm}^{-2}\cdot\text{ster}^{-1}$  for all detectors of the TES thermal bolometer, which can be used to estimate the calibration error of the TES thermal data. We integrate such a calibration error over emission angle and azimuth angle (Eq. 1) to get the corresponding uncertainty in the emitted power of Mars ( $\sim 1.18 \times 10^{-1}\ \text{Wm}^{-2}$ ).

Now we discuss the uncertainty related to filling observational gaps of the TES observations. Even though we average the TES data from MY 24 to 28, there are still observational gaps in emission angle and latitude that must be filled before we calculate the meridional profiles of Mars' emitted power. Based on



the uncertainty analysis in our study of Saturn's emitted power (8), we have the sum of unknown radiance in the observational gaps along a single latitude ( $P_{emit}(N)$ ) as

$$P_{emit}(N) = 2\pi \sum_{k=1}^N I(\delta_k) \cos \delta_k \sin \delta_k \Delta \delta = \sum_{k=1}^N c_k l_k, \quad [4]$$

where  $N$  is the number of the radiance at the unknown emission angles and  $I(\delta_k)$  is the radiance at the unknown emission angles ( $\delta_k$ ). In the above equation, we also simplify the equation with a coefficient  $c_k$ , which is represented by  $c_k = 2\pi \cos \delta_k \sin \delta_k \Delta \delta$ . Then, the total difference between the fitting radiance and the real radiance for all observational gaps along the latitude ( $P_{emit}(N)'$ ) can be expressed as

$$P_{emit}(N)' = \sum_{k=1}^N c_k l'_k, \quad [5]$$

where  $l'_k$  is the radiance difference between the fitting value and the real value at unknown emission angles.

The variance of  $P_{emit}(N)'$  is used to estimate the uncertainty of emitted power related to filling the observational gaps. The variance of the sum of multiple variables can be determined by the following equation (57):

$$\sigma^2[P_{emit}(N)'] = \sum_{k=1}^N c_k^2 \sigma_k^2 + 2 \sum_{i=2}^N \sum_{j=1}^{i-1} c_i c_j \sigma_{ij}^2, \quad [6]$$

where  $\sigma_k^2$  is the variance of the radiance difference  $l'_k$  and  $\sigma_{ij}^2$  is the covariance of the radiance difference at two different unknown emission angles with the two corresponding coefficients  $c_i$  and  $c_j$ .

As we discussed in the section on data processing, we mainly use the linear interpolation in the direction of emission angle to fill the observational gaps at each latitude. Here, we use the statistical characteristics of the observational data (i.e., the SD) to estimate the uncertainty related to filling observational gaps by the linear interpolation/extrapolation ( $\sigma_k^2$ ). The covariance  $\sigma_{ij}^2$  will disappear if we assume that the radiances at different unknown points are independent from each other. Then, Eq. 6 can be used to compute the uncertainty related to filling the observational gaps. *SI Appendix, Fig. S16* shows the meridional profiles of the uncertainty related to filling observations gaps for the four seasons.

We also include the interannual variations of Mars' thermal radiance into our estimate of the uncertainty of Mars' emitted power. If we assume that the interannual variations of Mars' thermal radiance does not significantly vary with emission angle, we can use the interannual variations of Mars' thermal radiance at  $0^\circ$  emission angle (*SI Appendix, Fig. S13*) to estimate the SD of Mars' emitted power. In other words, we assume that the ratio between the SD and mean of the interannual variations is the same between Mars' thermal radiance at  $0^\circ$  emission angle and Mars' emitted power. Based on the meridional profiles of Mars' emitted power, we can convert the ratio between the SD and mean of the interannual variations of Mars' thermal radiance at  $0^\circ$  emission angle (*SI Appendix, Fig. S14*) into the SD of the interannual variations of Mars' emitted power (*SI Appendix, Fig. S17*).

The estimated SD of the interannual variations of Mars' emitted power is further compared with the uncertainty related to filling observational gaps (*SI Appendix, Fig. S18*), which suggests they are comparable at most latitudes. The uncertainties related to the TES data calibration and filling observational gaps are combined with the estimated SD of the interannual variations of Mars' emitted power to estimate the total uncertainty of Mars' emitted power. Based on the error propagation of addition (61), we have the total uncertainty of Mars' thermal power as

$$\sigma_{total} = \sqrt{\sigma_{cal}^2 + \sigma_{gap}^2 + \sigma_{std}^2} \quad [7]$$

where  $\sigma_{cal}^2$ ,  $\sigma_{gap}^2$ , and  $\sigma_{std}^2$  are uncertainties related to data calibration, filling observational gaps, and the SD of the estimated interannual variations of Mars' emitted power. The meridional profiles of the total uncertainty in the TES measurements of Mars' emitted power at 2 PM/AM are provided in *SI Appendix, Fig. S19*, which are used in *SI Appendix, Figs. S8 and S9*. Then, we can use the error propagation theory (57) to get the uncertainty for the meridional profiles of daily-mean emitted power (Figs. 1 and 2). It should be mentioned that there are other possible error sources which are not considered. For example, the diurnal cycle of atmospheric temperature and its related temporal variations of emitted power also affect the diurnal cycle of Mars' emitted power, even though the surface primarily contributes to Mars' total emitted power. The atmospheric

boundary layer probably plays a dominant role in the atmospheric contribution to Mars' emitted power because of its relatively high temperature and density. However, retrieving global-scale temperature of boundary atmosphere from satellite observations is generally challenging due to the turbulent nature of the boundary layer. Furthermore, determining the diurnal cycle of atmospheric temperature in the boundary layer would require stricter observations and measurements.

Now, we discuss the uncertainty of the global-average emitted power. From Eq. 3, we know that the global-average emitted power is the sum of multiple variables. Again, we can use the analysis of the variance of the sum of multiple variables (57) to estimate the uncertainty of the global-average emitted power. Using the uncertainty of emitted power at each latitude and assuming the emitted power is independent at different latitudes, we have the uncertainty of the global-average emitted power as

$$\sigma^2(\bar{P}) = \sum_{i=1}^N c_i^2 \sigma^2(P_i). \quad [8]$$

Based on Eq. 8, we can compute the uncertainty of global-average emitted power of Mars for the four seasons. Likewise, we conduct a similar analysis for the uncertainties of hemispheric-average emitted power. For the Martian year with a global dust storm (MY25), we have the same uncertainty analysis except the interannual variations of Mars' emitted power are not considered. Finally, the error propagation theory (57) was applied to the four-season analysis to get the uncertainty of the annual-mean emitted power. All these uncertainties are shown in Figs. 1–4 and *SI Appendix, Figs. S8–S10 and Tables S1 and S2*.

**Mars' Global Albedo and Surface Temperature.** To determine the global- and hemispheric-average absorbed solar powers, we need the global and hemispheric averages of Mars' albedo. Then, the total solar flux on Mars (*SI Appendix, Fig. S1*) can be combined with the global and hemispheric albedo to get the global- and hemispheric-average absorbed solar powers. The spatial distribution of Mars albedo has been investigated by some previous studies (50–53). To be consistent with our TES analysis of Mars' emitted power, we use the global albedo (*SI Appendix, Fig. S20*) retrieved from the TES visible observations (51) to get the global- and hemispheric-average albedos. Please note that the global-average albedo ( $\sim 0.20$ ) from the TES study (51) is smaller than our estimated global-average albedo (0.241) by assuming the global radiant energy budget is balanced. It is possible that the TES albedo retrieved from visible observations underestimates Mars' albedo because the Lambert surface is assumed in retrieving the TES albedo (51). Considering the Lambert assumption possibly introduces systematical uncertainties over the two hemispheres, the albedo contrast between the two hemispheres, which is estimated based on the TES albedo, can probably represent the real hemispheric difference of Mars' albedo. We first calculate the hemispheric-average albedos based on the global map of Mars' albedo (*SI Appendix, Fig. S20*) provided in the previous TES study (51), which generates 0.224 and 0.175 for the NH-average and SH-average albedos, respectively. Then, we scale the hemispheric-average albedos by a factor (0.241/0.20) to make the global-average albedo equate to 0.241. Finally, we have the hemispheric-average albedos as 0.270 and 0.211 for the NH and SH, respectively. From the global-average albedo ( $\sim 0.241$ ) and the corresponding hemispheric-average albedos (i.e., 0.270 and 0.211 for the NH and SH respectively), we can compute the global and hemispheric absorbed solar powers.

The energy excesses in the SH in the Southern spring and summer (Fig. 4) can warm up the surface and hence the boundary atmosphere. Retrieving the atmospheric temperature in the boundary layer is generally difficult and has large uncertainty because of the turbulent nature of atmospheric boundary layer. Here, we examine the surface temperature based on the previous TES studies (e.g., ref. 51). The radiant energy budget analyzed in the main text (Fig. 4) does not include the season with a global dust storm (i.e., fall, MY25). Therefore, we also exclude the fall season in MY25 in our analysis of surface temperature. The TES-retrieved longitude-average surface temperature in MYs 24, 25, 26, and 27 are averaged into the four seasons, which is shown in *SI Appendix, Fig. S21*. We can see the significantly warm surface temperature in the SH for the Northern autumn and winter seasons (i.e., the Southern spring and summer seasons), which is consistent to the radiant energy excesses in the same region for the corresponding seasons.

**Data Availability.** All study data are included in the article and/or *SI Appendix*. Previously published data were used for this work (51). The

corresponding albedo data are publicly available on the Planetary Data System (PDS) at <https://pds-geosciences.wustl.edu/missions/mgs/tesspecial.html> and the Arizona State University Mars global dataset at [http://www.mars.asu.edu/data/tes\\_albedo/](http://www.mars.asu.edu/data/tes_albedo/)).

**ACKNOWLEDGMENTS.** E.C. and L.L. thank L.L.'s postdoc advisors, Dr. Barney J. Conrath, and Dr. Peter J. Gierasch, who encouraged him to begin the studies

of the radiant energy budgets of planets and their moons. We also thank the mission teams of Mars Global Surveyor, Curiosity, and InSight for processing the great datasets of Mars' atmosphere and surface, which make our analysis possible. In addition, we gratefully acknowledge Patrick Fry at the University of Wisconsin-Madison and Sylvain Piqueux at NASA Jet Propulsion Laboratory for providing assistance in conducting the research.

- J. P. Peixoto, A. H. Oort, *Physics of Climate* (American Institute of Physics, 1992).
- B. J. Conrath, R. A. Hanel, R. E. Samuelson, "Thermal structure and heat balance of the outer planets" in *Origin and Evolution of Planetary and Satellite Atmospheres*, S. K. Atreya, J. B. Pollack, M. S. Mathews, Eds. (The University of Arizona Press, 1989), pp. 513-538.
- R. A. Hanel, B. J. Conrath, D. E. Jennings, R. E. Samuelson, *Exploration of the Solar System by Infrared Remote Sensing* (Cambridge University Press, 2003).
- J. T. Kiehl, K. E. Trenberth, Earth's annual global mean energy budget. *Bull. Am. Meteorol. Soc.* **78**, 197-208 (1997).
- K. E. Trenberth, J. T. Fasullo, J. T. Kiehl, Earth's global energy budget. *Bull. Am. Meteorol. Soc.* **90**, 311-324 (2009).
- J. Hansen *et al.*, Earth's energy imbalance: Confirmation and implications. *Science* **308**, 1431-1435 (2005).
- A. P. Ingersoll, Atmospheric dynamics of the outer planets. *Science* **248**, 308-315 (1990).
- L. Li *et al.*, Emitted power of Saturn. *J. Geophys. Res.* **115**, E11002 (2010).
- L. Li *et al.*, The global energy balance of Titan. *Geophys. Res. Lett.* **38**, L23201 (2011).
- L. Li *et al.*, Less absorbed solar energy and more internal heat for Jupiter. *Nat. Commun.* **9**, 3709 (2018).
- E. C. Creedy *et al.*, Titan's energy imbalance during the Cassini epoch. *Geophys. Res. Lett.* **48**, e2021GL095356 (2021).
- E. C. Creedy *et al.*, Seasonal variations of Titan's brightness. *Geophys. Res. Lett.* **46**, 13649-13657 (2019).
- K. E. Trenberth, J. T. Fasullo, M. A. Balmaseda, Earth's global energy budget. *J. Clim.* **27**, 3129-3144 (2014).
- L. Li, Dimming Titan revealed by the Cassini observations. *Sci. Rep.* **5**, 8239 (2015).
- D. A. Paige, A. P. Ingersoll, Annual heat balance of Martian polar caps: Viking observations. *Science* **228**, 1160-1168 (1985).
- D. A. Paige, J. E. Bachman, K. D. Keegan, Thermal and albedo mapping of the polar regions of Mars using Viking thermal mapper observations: 1. North polar region. *J. Geophys. Res. Planets* **99**, 25959-25991 (1994).
- G. M. Martinez *et al.*, The surface energy budget at gale crater during the first 2500 sols of the Mars science laboratory mission. *J. Geophys. Res. Planets* **119**, 1822-1838 (2014).
- R. M. Haberle, Estimating the power of Mars' greenhouse effect. *Icarus* **223**, 619-620 (2013).
- P. L. Read *et al.*, Global energy budgets and 'Trenberth diagrams' for the climates of terrestrial and gas giant planets. *Q. J. R. Meteorol. Soc.* **142**, 703-720 (2016).
- R. Goody, Maximum entropy production in climate theory. *J. Atmos. Sci.* **64**, 2735-2739 (2007).
- G. Schubert, J. L. Mitchell, "Planetary atmospheres as heat engines" in *Comparative Climatology of Terrestrial Planets*, S. J. Mackwell, A. A. Simon-Miller, J. W. Harder, M. A. Bullock, Eds. (The University of Arizona Press, 2014), pp. 181-191.
- A. L. Albee, F. D. Palluconi, R. E. Arvidson, Mars global surveyor mission: Overview and status. *Science* **279**, 1671-1672 (1998).
- A. L. Albee, Introduction to the special section: The Mars global surveyor mission. *J. Geophys. Res. Planets* **106**, 23289 (2001).
- P. R. Christensen *et al.*, Results from the Mars global surveyor thermal emission spectrometer. *Science* **279**, 1692-1698 (1998).
- R. T. Clancy *et al.*, An intercomparison of ground-based millimeter, MGS TES, and Viking atmospheric temperature measurements: Seasonal and interannual variability of temperature and dust loading in the global Mars atmosphere. *J. Geophys. Res.* **105**, 9553-9572 (2000).
- M. D. Smith, B. J. Conrath, J. C. Pearl, P. R. Christensen, Thermal Emission Spectrometer observations of Martian planet-encircling dust storm 2001A. *Icarus* **157**, 259-263 (2002).
- M. D. Smith, Interannual variability in TES atmospheric observations of Mars during 1999-2003. *Icarus* **167**, 148-165 (2004).
- M. A. Gurwell, E. A. Bergin, G. J. Melnick, V. Tolls, Mars surface and atmospheric temperature during the 2001 global dust storm. *Icarus* **175**, 23-31 (2005).
- M. J. Strausberg, H. Wang, M. I. Richardson, S. P. Ewald, A. D. Toigo, Observations of the initiation and evolution of the 2001 Mars global dust storm. *J. Geophys. Res. Planets* **110**, E2006 (2005).
- C. Cornwall, T. N. Titus, Spatial and temporal distributions of Martian north polar cold spots before, during, and after the global dust storm of 2001. *J. Geophys. Res. Planets* **114**, 10.1029/2008JE003243 (2009).
- L. Li *et al.*, Emitted power of Jupiter based on Cassini CIRS and VIMS observations. *J. Geophys. Res.* **117**, E11002 (2012).
- P. M. Streeter, S. R. Lewis, M. R. Patel, J. A. Holmes, D. M. Kass, Surface warming during the 2018/Mars year 34 global dust storm. *Geophys. Res. Lett.* **46**, e2019GL083936 (2020).
- J. R. Barnes *et al.*, "The global circulation" in *The Atmosphere and Climate of Mars*, R. M. Haberle, R. T. Clancy, F. Forget, M. D. Smith, R. W. Zurek, Eds. (Cambridge University Press, 2017), pp. 229-294.
- S. D. Guzewich *et al.*, Mars Science Laboratory observations of the 2018/Mars year 34 global dust storm. *Geophys. Res. Lett.* **46**, 71-79 (2019).
- M. D. Smith, THEMIS observations of the 2018 Mars global dust storm. *JGR: Planets* **124**, 2929-2944 (2019).
- A. Kleinböhl *et al.*, Diurnal variations of dust during the 2018 global dust storm observed by the Mars Climate Sounder. *JGR: Planets* **125**, e2019JE006115 (2020).
- M. A. Kahre *et al.*, "The Mars dust cycle" in *The Atmosphere and Climate of Mars*, R. M. Haberle, R. T. Clancy, F. Forget, M. D. Smith, R. W. Zurek, Eds. (Cambridge University Press, 2017), pp. 295-337.
- B. A. Cantor, P. B. James, M. Caplinger, M. J. Wolff, Martian dust storms: 1999 Mars orbiter camera observations. *JGR: Planets* **106**, 23653-23687 (2001).
- H. Jacobowitz, W. L. Smith, H. B. Howell, F. W. Nagle, J. R. Hickey, The first 18 months of planetary radiation budget measurements from the Nimbus 6 ERB experiment. *J. Atmos. Sci.* **36**, 501-507 (1979).
- S. K. Yang, Y. T. Hou, A. J. Miller, K. A. Campana, Evaluation of the earth radiation budget in NCEP-NCAR reanalysis with ERBE. *J. Clim.* **12**, 477-493 (1999).
- S. R. Lewis, M. Collins, P. L. Read, A climate database for Mars. *JGR: Planets* **104**, 24177-24194 (1999).
- P. G. Irwin *et al.*, The NEMESIS planetary atmosphere radiative transfer and retrieval tool. *J. Quant. Spectrosc. Radiat. Transf.* **109**, 61136-61150 (2008).
- J. Grotzinger *et al.*, Mars science laboratory mission and science investigation. *Space Sci. Rev.* **170**, 5-56 (2012).
- G. M. Martinez *et al.*, The modern near-surface Martian climate: A review of in-situ meteorological data from Viking to curiosity. *Space Sci. Rev.* **212**, 295-338 (2017).
- A. Spiga *et al.*, Atmospheric science with insight. *Space Sci. Rev.* **214**, 109 (2018).
- M. J. Wolff *et al.*, "Radiative process: Techniques and applications" in *The Atmosphere and Climate of Mars*, R. M. Haberle, R. T. Clancy, F. Forget, M. D. Smith, R. W. Zurek, Eds. (Cambridge University Press, 2017), pp. 106-171.
- L. K. Pleskot, H. H. Kieffer, The infrared photometric function of Mars and its bolometric albedo. *Icarus* **30**, 341-359 (1977).
- K. Holliday, *Introductory Astronomy* (Wiley, New York, 1999).
- R. Kandel, M. Viollier, Planetary radiation budgets. *Space Sci. Rev.* **120**, 1-26 (2005).
- P. R. Christensen, Global albedo variations on Mars: Implications for active aeolian transport, deposition, and erosion. *J. Geophys. Res.* **93**, 7611-7624 (1988).
- P. R. Christensen *et al.*, The Mars Global Surveyor Thermal Emission Spectrometer experiment: Investigation description and surface science results. *J. Geophys. Res.* **106**, 23823-23871 (2001).
- M. Vincendon, J. Audouard, F. Altieri, A. Ody, Mars Express measurements of surface albedo changes over 2004-2010. *Icarus* **251**, 145-163 (2015).
- D. F. Wellington, J. F. Bell III, Patterns of surface albedo changes from Mars Reconnaissance Orbiter Mars Color Imager (MARCI) observations. *Icarus* **349**, 113766 (2020).
- F. Forget, F. Hourdin, R. Fournier, C. Hourdin, O. Talagrand, Improved general circulation models of the Martian atmosphere from the surface to above 80 km. *J. Geophys. Res.* **104**, 24155-24176 (1999).
- C. E. Newman, S. R. Lewis, P. L. Read, F. Forget, Modeling the Martian dust cycle, Representations of dust transport processes. *J. Geophys. Res.* **107**, 5123 (2002).
- S. Basu, M. I. Richardson, R. J. Wilson, Simulation of the Martian dust cycle with the GFDL Mars GCM. *J. Geophys. Res.* **109**, E11006 (2004).
- R. J. Wilson, S. R. Lewis, L. Montabone, M. D. Smith, Influence of water ice clouds on Martian tropical atmospheric temperatures. *Geophys. Res. Lett.* **35**, L07202 (2008).
- S. Chandrasekhar, *Radiative Transfer* (Oxford University Press, 1950).
- R. M. Goody, Y. L. Yung, *Atmospheric Radiation: Theoretical Basis* (Oxford University Press, 1989).
- A. P. Ingersoll *et al.*, Pioneer 11 infrared radiometer experiment: The global heat balance of Jupiter. *Science* **188**, 472-473 (1975).
- P. R. Bevington, D. K. Robinson, *Data Reduction and Error Analysis for the Physical Sciences* (McGraw-Hill, ed. 3, 2003).